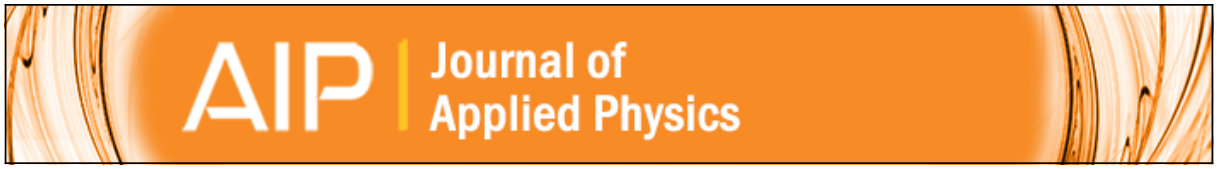


# Structure and thermoelectric properties of EuTi(O,N)3±

L. Sagarna, K. Z. Rushchanskii, A. Maegli, S. Yoon, S. Populoh, A. Shkabko, S. Pokrant, M. Ležai, R. Waser, and A. Weidenkaff

Citation: Journal of Applied Physics **114**, 033701 (2013); doi: 10.1063/1.4813098
View online: http://dx.doi.org/10.1063/1.4813098
View Table of Contents: http://scitation.aip.org/content/aip/journal/jap/114/3?ver=pdfcov
Published by the AIP Publishing

**Articles you may be interested in**

Low temperature dielectric properties of YMn 0.95 Ru 0.05 O 3
AIP Conf. Proc. **1512**, 1238 (2013); 10.1063/1.4791499

Electronic structure and thermoelectric properties of nanostructured EuTi1 x Nb x O3 (x=0.00; 0.02)
Appl. Phys. Lett. **101**, 033908 (2012); 10.1063/1.4737872

Thermoelectric properties of Yb x Eu 1 x Cd 2 Sb 2
J. Chem. Phys. **133**, 194701 (2010); 10.1063/1.3501370

Effect of antisite defects on band structure and thermoelectric performance of ZrNiSn half-Heusler alloys
Appl. Phys. Lett. **96**, 152105 (2010); 10.1063/1.3396981

On the magnetism, thermal- and electrical transport of SrMoO 2 N
J. Appl. Phys. **105**, 023522 (2009); 10.1063/1.3067755


[This article is copyrighted as indicated in the article. Reuse of AIP content is subject to the terms at: http://scitation.aip.org/termsconditions. Downloaded to ] IP: 134.94.122.242 On: Thu, 03 Apr 2014 08:07:48

# Structure and thermoelectric properties of $EuTi(O,N)_{3\pm\delta}$

L. Sagarna,[1] K. Z. Rushchanskii,[2] A. Maegli,[1] S. Yoon,[1] S. Populoh,[1] A. Shkabko,[1,3] S. Pokrant,[1] M. Ležaić,[2] R. Waser,[3] and A. Weidenkaff[1]
[1]*Empa – Swiss Federal Laboratories for Materials Science and Technology, Solid State Chemistry and Catalysis, Überlandstrasse 129, CH-8600 Dübendorf, Switzerland*
[2]*Forschungszentrum Jülich GmbH and JARA Peter Grünberg Institut (PGI-1), Quantum Theory of Materials, 52425 Jülich, Germany*
[3]*Forschungszentrum Jülich GmbH, Peter Grünberg Institut (PGI-7), Electronic Materials, 52425 Jülich, Germany*

(Received 17 April 2013; accepted 18 June 2013; published online 15 July 2013)

After partial substitution of nitrogen for oxygen in $EuTiO_3$, the crystal structure, thermoelectric properties, morphology, and electronic structure of the products were analyzed and compared with pristine $EuTiO_3$. The space group of $EuTi(O,N)_{3\pm\delta}$ was orthorhombic *Pnma* due to the tilt and rotation of the anion octahedra, compared to cubic $Pm\bar{3}m$ of $EuTiO_3$ (at room temperature). The thermoelectric properties of oxynitride polycrystalline bodies sintered in three different ways were investigated in the temperature range of $300\,K < T < 950\,K$. The Seebeck coefficients ($S$) of the oxynitrides were lower compared with the oxide, and the electrical resistivities ($\rho$) were increased about one order of magnitude. The activation energies ($E_A$) indicated a larger band gap of $EuTi(O,N)_{3\pm\delta}$ when compared to the pristine $EuTiO_3$ ($\sim$1.3 eV compared to 0.98 eV). A morphological characterization by transmission electron microscopy and scanning electron microscopy illustrated intrinsic nanopores within the individual particles and weak grain-interconnections indicating poor intergrain electron transport. *Ab initio* calculations of the electronic structures confirmed a larger band gap of the distorted crystal structure of the oxynitride and showed a decrease of the density of states at the Fermi level, explaining the reduction of the measured $S$. © *2013 AIP Publishing LLC*. [http://dx.doi.org/10.1063/1.4813098]

## I. INTRODUCTION

Transition metal oxides with perovskite structure are attractive due to their strong electron correlations and their wide range of properties and applications. Among these, $EuTiO_3$ shows interesting magnetic and electric properties.[1–3] Katsufuji and Takagi[4] found coupling between magnetism and dielectric properties and demonstrated a possible control of the dielectric constant by a magnetic field and of the magnetization by an electric field. At $T_N = 5.5\,K$, the $Eu^{2+}$ moments ($J = S = 7/2$) order in a G-type antiferromagnetic structure.[5] At room temperature, $EuTiO_3$ has the cubic space group $Pm\bar{3}m$. A second-order phase transition from $Pm\bar{3}m$ to $I4/mcm$ at $T_c = 235\,K$ was found recently and was associated to a singularity in the specific heat.[6] Recent theoretical[7] and experimental[3,8] investigations show that the ground state crystal symmetry of pristine $EuTiO_3$ is lower than cubic $Pm\bar{3}m$. The physical and chemical properties of $EuTiO_3$ can be tuned by cation or anion substitutions and several cationic substitutions have been investigated, e.g., $Sr_{1-x}Eu_xTiO_3$ (Ref. 9) and $(Eu,Ba)TiO_3$.[10,11] The thermoelectric properties of $EuTiO_3$ were studied and a high Seebeck coefficient ($S$) was found ($-1053\,\mu V/K$ at 300 K). The electrical conductivity ($\sigma$) was enhanced by partial Nb substitution at the Ti site, leading to a thermoelectric figure of merit ($ZT$) of $EuTi_{0.98}Nb_{0.02}O_{3\pm\delta}$ of $ZT = 0.4$ at $T = 1040\,K$.[12]

Anion (i.e., oxygen) substitutions are less commonly used than cation substitutions due to their lower stability[13] and more complex synthesis methods.[14] However, the partial replacement of oxygen by nitrogen forming oxynitrides can lead to very interesting electronic and optical properties.[15] The higher electric charge of the nitride ion ($N^{3-}$) compared to the oxide ion ($O^{2-}$) leads to a charge compensation process and very often to the formation of new compounds with transition metals in higher oxidation states.[15] Magnetoresistance can be induced when nitrogen enables the stabilization of high oxidation states of the transition metal, as in the case of $EuWO_{1+x}N_{2-x}$.[16] In oxynitrides, the cubic perovskite crystal structure is generally distorted due to tilting and/or rotation of the anion octahedra. For example, when converting $CaTaO_3$ into $CaTaO_2N$ the space group changes from $Pm\bar{3}m$ to *Pnma* due to octahedral rotation and tilting[17] and the synthesis of $SrTi_{1-x}Nb_x(O,N)_3$ compounds also induces octahedral rotation resulting in $I4/mcm$ space group.[18] Electron diffraction (ED) studies of $EuMO_2N$ and $SrMO_2N$ (M = Nb, Ta) showed symmetry breaking of $I4/mcm$ and proved $I112/m$ to be the correct space group.[19]

In this work, the effect of nitridation on $EuTiO_3$ is reported. Crystallographic studies are performed in order to study the space group symmetry of $EuTi(O,N)_{3\pm\delta}$. The oxidation states of the cations are studied by X-ray photoelectron spectroscopy (XPS). Three different ammonolysis routes are used in order to compare the nitrogen contents and the different densification processes of the oxynitride pellets. Electrical resistivity, Seebeck coefficient and thermal conductivity ($\kappa$) of $EuTi(O,N)_{3\pm\delta}$ are measured and compared to $EuTiO_3$. In addition, we study the morphology of the oxynitride grains and of the sintered samples in order to understand the nitridation process and its influence on the thermoelectric properties. *Ab initio* calculations of the

 © 2013 AIP Publishing LLC

[This article is copyrighted as indicated in the article. Reuse of AIP content is subject to the terms at: http://scitation.aip.org/termsconditions. Downloaded to ] IP: 134.94.122.242 On: Thu, 03 Apr 2014 08:07:48

electronic density of states are performed in order to compare the theoretical results with the experimental findings.

## II. EXPERIMENTAL METHODS

$EuTiO_3$ precursor powders were prepared by solid-state reaction of $Eu_2O_3$ (99.9% purity; *Metall Rare Earth Limited*) and $TiO_2$ (puriss.; *Sigma-Aldrich*). A stoichiometric mixture of the powders was ball milled and heated at 1000 °C for 10 h in a flowing mixture of 5% $H_2$/Ar at a flow rate of 100 ml/min. X-ray diffraction showed that phase pure $EuTiO_3$ was obtained. The nitridation of the oxide precursors was carried out by thermal ammonolysis in $NH_3$ in an alumina tube reactor at atmospheric pressure and at $T = 950$ °C. A partial decomposition of ammonia takes place at the surface of the oxides, forming active nitriding species (N, NH, $NH_2$) and molecular hydrogen.[20] The latter reacts with the lattice oxygen to form water, while nitrogen is introduced into the lattice. $H_2$ might cause reduction of the cations. Three different routes were followed for the preparation of the oxynitride pellets in order to test different sintering processes. The first two groups of oxide powders were ammonolyzed for 10 h at 950 °C in an ammonia flow of 100 ml/min. The ammonolyzed powders were reground and pressed into disk shaped pellets (10 mm diameter and 2 mm thick) using first $2{\cdot}10^4$ Pa uniaxial pressure, and then $1.8{\cdot}10^8$ Pa isostatic pressure. A first group of pressed disks [group (I)] was annealed in the same alumina tube reactor for 1 h at 950 °C in an ammonia flow of 100 ml/min and a second group [group (II)] for 10 h under the same conditions. As it is known from previous studies on oxynitrides, the sintering of pressed powder typically results in highly porous pellets.[21] Therefore, the last oxynitride group [group (III)] was prepared directly by ammonolysis of pressed $EuTiO_3$ pellets, with the aim to achieve a higher relative density than that of the oxynitride groups (I) and (II). Thus, the oxide powder used for the synthesis of group (III) was pressed with $2{\cdot}10^4$ Pa uniaxial pressure and then $1.8{\cdot}10^8$ Pa isostatic pressure, and sintered at 1000 °C for 10 h in reducing atmosphere. The resulting pellets were ammonolyzed for 10 h at T = 950 °C in an ammonia flow of 100 ml/min. Prior to pelletizing, powders of groups (I) and (II) were studied by X-ray, neutron and electron diffraction and thermogravimetric analysis (TGA). The sintering and densification of the oxynitrides were more problematic than those of the oxides since the samples tended to be pulverized during the preparation. The calculation of the densities was based on the dimension and weight of the pellets.

The powder neutron diffraction (ND) patterns were collected with a high-resolution powder diffractometer for thermal neutrons located at the Swiss Spallation Neutron Source at the Paul Scherrer Institut (Villigen, Switzerland). The powder sample was placed inside a double-wall vanadium cylinder of 9 mm outer diameter, 7 mm inner diameter, and 50 mm length in order to minimize the large neutron absorption of Eu. The measurement was carried out with a neutron wavelength of 1.1545 Å in an angular range of $4.05° < 2\theta < 164.90°$ with a step size of 0.05°. The neuron diffraction patterns were analyzed by the Le Bail method[22] and Rietveld refinement[23] using the program *FULLPROF*.[24] The background was simulated by linear interpolation based on 46 points and the Thompson-Cox-Hastings pseudo-Voigt function[25] was chosen as profile function.

Since electron diffraction (ED) patterns can detect superstructures in individual crystallites, we carried out ED and high resolution (HR) experiments using a JEOL JEM-2200FS transmission electron microscope (TEM). The microscope was equipped with a field emission gun (FEG) with ZrO/W Schottky Emitter and the acceleration voltage used was 200 kV. Investigations on the grain morphology were carried out with a Philips CM30 microscope operating at 300 kV. The powders, previously ground in ethanol, were deposited on TEM 3 mm diameter grids (Cu 200 mesh) with a Carbon holey film.

XPS spectra were acquired on a Physical Electronics (PHI) Quantum 2000 photoelectron spectrometer using monochromated Al-$K_\alpha$ radiation and a hemispherical capacitor electron-energy analyzer equipped with a channel plate and a position-sensitive detector. The electron take-off angle was 45° and the analyzer was operated in the constant pass energy mode for all the measurements. The analyzer pass energy was set to 46.95 eV with a step size of 0.2 eV. Two specimens of each sample were prepared, top and cross section oriented, in order to obtain signals from the two different parts of the pellets. Spectra were acquired before and after $Ar^+$ sputtering with acceleration energy of 2 kV. Quantitative analysis of the sputtered samples was performed with the CasaXPS software using the relative sensitivity factors provided by the PHI MultiPak library. The C 1*s* signal position at a binding energy of 284.8 eV was used as an internal standard to compensate for any charging effects of the unsputtered samples. After calibration, the peak position of the O 1*s* signal of the unsputtered samples was taken as the calibration binding energy for the sputtered samples.

Thermal stability of the oxynitrides was studied by TGA, with a Netzsch STA 409 CD thermobalance coupled to a Netzsch QMS 403 C Aeolos mass spectrometer (MS). The measurements were performed in the temperature range $313\,K < T < 1273\,K$ in reducing atmosphere (5% $H_2$/Ar at 50 ml/min).

The electrical resistivity ($\rho$) and Seebeck coefficient ($S$) were determined with a RZ200li system (Ozawa Science) in the temperature range $300\,K < T < 950\,K$. $\kappa$ was calculated from the thermal diffusivity ($\alpha$) and specific heat ($C_p$). $\alpha$ was determined by Laser Flash Analysis (LFA) with a Netzsch LFA 457 Microflash. $C_p$ was measured by Differential Scanning Calorimetry (DSC) using a Netzsch DSC 404 C Pegasus apparatus. The thermoelectric properties of $EuTi(O,N)_{3\pm\delta}$ were compared to the results of $EuTiO_3$ from previous studies.[12]

The morphology of the pressed samples was studied by scanning electron microscopy (SEM) with a XL30 ESEM (FEI) operating at 10 kV with a secondary electron (SE) detector. Each sample was placed on an aluminum SEM holder with a carbon double side adhesive disk, and coated with

[This article is copyrighted as indicated in the article. Reuse of AIP content is subject to the terms at: http://scitation.aip.org/termsconditions. Downloaded to ] IP: 134.94.122.242 On: Thu, 03 Apr 2014 08:07:48

carbon in order to ensure conductivity of the electrons coming from the beam.

## III. CALCULATIONS

Calculations were performed with the Vienna *ab-initio* Simulation Package (VASP) code[26,27] with projector augmented wave pseudopotentials.[28] We considered the following valence-electron configurations: $5s^2 5p^6 4f^7 6s^2$ for Eu, $3s^2 3p^6 3d^2 4s^2$ for Ti, $2s^2 2p^4$ for oxygen and $2s^2 2p^3$ for nitrogen. The Heyd-Scuseria-Ernzerhof (HSE) hybrid functional[29] was used. This function accounts for the strong electron correlations effects of the Eu *f* and the Ti *d* shells, and can describe precisely the possible localization of the hole in the N *p* shells. Energy gap and the positions of the impurity levels are described more precisely with the HSE than with any other local functional.[30] In the calculations, we used a kinetic energy cutoff of 500 eV. The electronic structure was calculated based on a $6 \times 6 \times 6$ Γ-centered *k*-point mesh[31] for pristine $EuTiO_3$, and $2 \times 2 \times 2$ *k*-point mesh of a 40-atomic $2 \times 2 \times 2$ supercell with a nitrogen impurity. The experimental crystal structure parameters were used; $a = 3.90$ Å was taken as the lattice parameter of the cubic phase of $EuTiO_3$ (Ref. 4) and the structural parameters of the *Pnma* phase are listed in Tables I and II. The resulting partial density of states (PDOS) contributed by different atoms, as well as the total density of states (DOS) of pristine $EuTiO_3$ and $EuTi(O,N)_{3\pm\delta}$ are presented in Figs. 10 and 12, respectively. We define the zero energy level at the top of the valence band ($E_v = 0$ eV).

## IV. RESULTS AND DISCUSSION

The XRD pattern of the oxynitride powder $EuTi(O,N)_{3\pm\delta}$ corresponded to the cubic $Pm\bar{3}m$ space group with cell parameter $a = 3.905$ Å, equivalent to pristine $EuTiO_3$.[4] However, the XRD pattern is dominated by the contribution of the heavy elements ($Eu^{2+}$ and $Ti^{4+}$) making it difficult to obtain structural information about the exact atomic positions, individual atomic displacement parameters (ADPs) and site-occupation factors of the anions.[19,32] As the X-ray form factors of $O^{2-}$ and $N^{3-}$ are nearly identical, it is especially demanding to detect space group variations caused by changes in the anionic crystal lattice. ND was employed for this purpose, since it offers high O/N scattering contrast due to very different neutron scattering lengths (N, 9.36 fm; O, 5.81 fm). Fig. 1 shows the powder ND pattern and Rietveld refinement profile of $EuTi(O,N)_{3\pm\delta}$. Profile matching of the main structure was performed with Le Bail method according to three possible structural models: cubic ($Pm\bar{3}m$), tetragonal ($I4/mcm$) and orthorhombic (*Pnma*). The reliability factors and $\chi^2$ factor were found to be higher for the cubic and the tetragonal models than for *Pnma*, suggesting a better fit for the latter space group. TiN was identified as a minor secondary phase (<1 wt. %, estimated by quantitative phase analysis[33]) and the reflections of the vanadium cylinder sample holder can also be observed in the pattern (see Fig. 1 reflexes *b* and *c*). Rietveld refinement was carried out for the three possible space groups of $EuTi(O,N)_{3\pm\delta}$ and neither $Pm\bar{3}m$ nor $I4/mcm$ could be satisfactorily refined. Rietveld refinement with *Pnma* showed the most successful fit (reliability factors and $\chi^2$ factor are shown in Table I) indicating that $EuTi(O,N)_{3\pm\delta}$ has *Pnma* space group symmetry ($a = 5.519$ Å; $b = 7.802$ Å; $c = 5.526$ Å). The structural

TABLE I. Crystallographic parameters and structural refinements.

| Chemical formula | $EuTi(O,N)_{3\pm\delta}$ |
|---|---|
| Radiation | Neutron |
| Crystal system | Orthorhombic |
| Space group | *Pnma* |
| Z | 4 |
| Lattice parameter *a* (Å) | 5.5187(3) |
| Lattice parameter *b* (Å) | 7.8020(5) |
| Lattice parameter *c* (Å) | 5.5261(5) |
| $R_p$ (%) | 1.84 |
| $R_{wp}$ (%) | 2.33 |
| $R_{exp}$ (%) | 1.71 |
| $\chi^2$ | 1.87 |
| Wavelength (Å) | 1.1545 |
| 2θ range (deg) | 3.95–164.90 |
| 2θ step width (deg) | 0.05 |

TABLE II. Crystal structural parameters of $EuTi(O,N)_{3\pm\delta}$ determined from the Rietveld refinement of the powder neutron diffraction pattern.

| Atom | Site | *x* | *y* | *z* | $B_{iso}$ (Å$^2$) | *g*[a] |
|---|---|---|---|---|---|---|
| Eu | 4*c* | 0.4987(9) | 1/4 | 0.0041(31) | 0.800(41) | 0.5 |
| Ti | 4*a* | 0 | 0 | 0 | 0.578(38) | 0.5 |
| O1/N1 | 4*c* | 0.5331(15) | 1/4 | 0.4771(21) | 1.600(145) | 0.482/0.018[b] |
| O2/N2 | 8*d* | 0.2418(14) | 0.0030(14) | 0.2588(13) | 0.3431(261) | 1.000/0.000[c] |

[a]*g*: Occupation factor.
[b]Linear constrain: g(O1) + g(N1) = 0.5.
[c]Linear constrain: g(O2) + g(N2) = 1.0 and the occupation factor of O2/N2 is fixed during the refinement. Otherwise, the refinement did not converge.

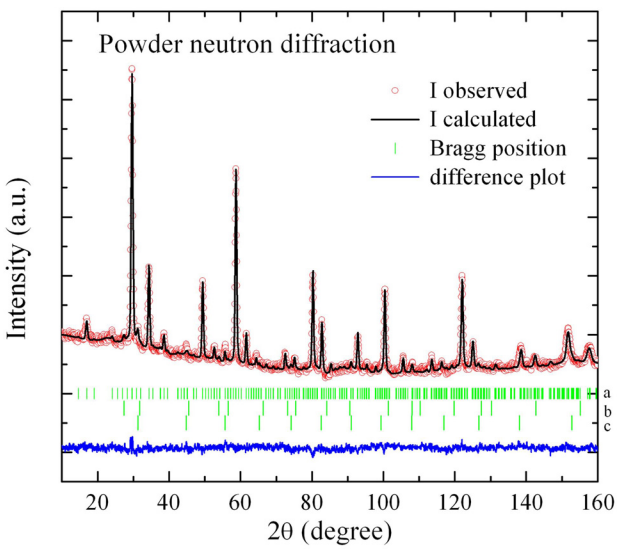


FIG. 1. Powder neutron diffraction pattern (neutron wavelength: 1.1545 Å) and Rietveld refinement plot of $EuTi(O,N)_{3\pm\delta}$ obtained at room temperature. The difference plot of observed and calculated diffraction profiles is shown beneath and the Bragg positions are given by short vertical tick markers ([a]$EuTi(O,N)_{3\pm\delta}$, [b]TiN, [c]V).

[This article is copyrighted as indicated in the article. Reuse of AIP content is subject to the terms at: http://scitation.aip.org/termsconditions. Downloaded to ] IP: 134.94.122.242 On: Thu, 03 Apr 2014 08:07:48

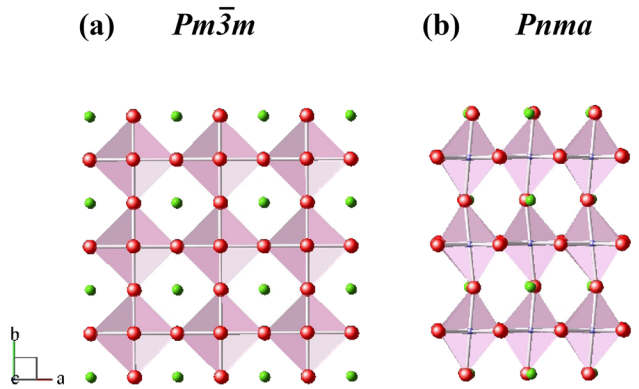


FIG. 2. (a) Cubic structure of $EuTiO_3$ and (b) orthorhombic structure of $EuTi(O,N)_{3\pm\delta}$ due to the rotation and tilt of the anion octahedra (view along the [001] direction).

change originates from rotation and tilting of the oxygen octahedra of the perovskite as shown in Fig. 2. The refined structural parameters deduced from the ND pattern are summarized in Tables I and II. Applying a linear constrain on the anion site-occupancy factors of $g(O1) + g(N1) = 0.5$ and $g(O2) + g(N2) = 1.0$, the refined values revealed a full occupation of N only at the O1/N1 site. The content of oxygen and nitrogen was determined to be $2.96 \pm 0.04$ and $0.04 \pm 0.04$, respectively. Even though the nitrogen content is be very low compared with other reported oxynitrides,[34] the effect on the crystal structure is clearly detectable. Tanaka and Ōnuki[35] reported on the strong influence of the 4*f* electrons of Ce on the electron density distribution (EDD) and the crystal structure of $CeB_6$ as a function of temperature. Similarly in our case, Eu 4*f* electrons can be affected by Eu-N bonds and change the EDD affecting the crystal structure.

The $EuTi(O,N)_{3\pm\delta}$ powder was analyzed by electron diffraction (ED) to verify the structural information obtained from neutron diffraction. Fig. 3 shows the ED pattern [Fig. 3(a)] and the high resolution micrograph at the same crystal orientation of a typical crystallite [Fig. 3(b)]. The first indexing attempt of the diffraction spots resulted in *I*4/*mcm* space group along the $[\bar{1}\,\bar{1}\,1]$ zone axis (white indexes). However, the ED revealed a symmetry breaking indicated by a weaker secondary pattern (yellow arrows and indexes). The secondary spots could be successfully indexed with the *Pnma* space group. These results confirm the orthorhombic *Pnma* space group of $EuTi(O,N)_{3\pm\delta}$, in agreement with ND.

TABLE III. Oxygen and nitrogen stoichiometry determined by XPS quantification of the O 1*s* and N 1*s* peaks.

| Sintered sample | | Stoichiometry |
|---|---|---|
| Group (I): $EuTi(O,N)_{3\pm\delta}$ pellet 1 h sintered | Position A | $EuTiO_{2.945}N_{0.095}$ |
| | Position B | $EuTiO_{2.970}N_{0.090}$ |
| Group (II): $EuTi(O,N)_{3\pm\delta}$ pellet 10 h sintered | Position A | $EuTiO_{2.735}N_{0.095}$ |
| | Position B | $EuTiO_3N_{0.070}$ |
| Group (III): $EuTiO_3$ pellet 10 h sintered | Position A | $EuTiO_{2.965}N_{0.075}$ |
| | Position B | $EuTiO_{2.965}N_{0.065}$ |

The O/N content was also determined by XPS quantification of the O 1*s* and N 1*s* peaks. The N 1*s* peak is located at $E_b = 395.7$ eV, indicating $N^{3-}$ oxidation state, like in lattice nitrogen in N-doped $TiO_2$.[36] The O 1*s* peak at $E_b = 529.4$ eV reveals a shoulder at higher binding energies arising from hydroxyl groups at the surface. Similar results were obtained with $SrTiO_3$, where the two peaks at ~530.0 eV and ~531.6 eV could be associated with lattice oxygen and OH groups, respectively.[37] Two different positions were studied for all sample groups, one located at the surface of the pellet (position A) and the other one at the cross section (position B) (Table III). Quantification of the atomic percentage with given sensitivity factors is estimated to involve an absolute error of around 10%. Group (III) has a slightly lower N content than the other powders, since N diffusion is restricted in the already pressed oxide pellet. Samples (I) and (III) show a slight anion excess which might be either due to experimental error of the XPS quantification or caused by a slight surface reoxidation of Eu. Nevertheless, these O/N calculated values are in the same range as the ones refined from neutron diffraction. The low N incorporation into the $EuTiO_3$ lattice is attributed to the strong reducing conditions during ammonolysis arising from the decomposition of ammonia into nitrogen species and $H_2$. Since $Eu^{3+}$ ions are required for N incorporation, the reduction to $Eu^{2+}$ is a competing reaction diminishing the final N content.

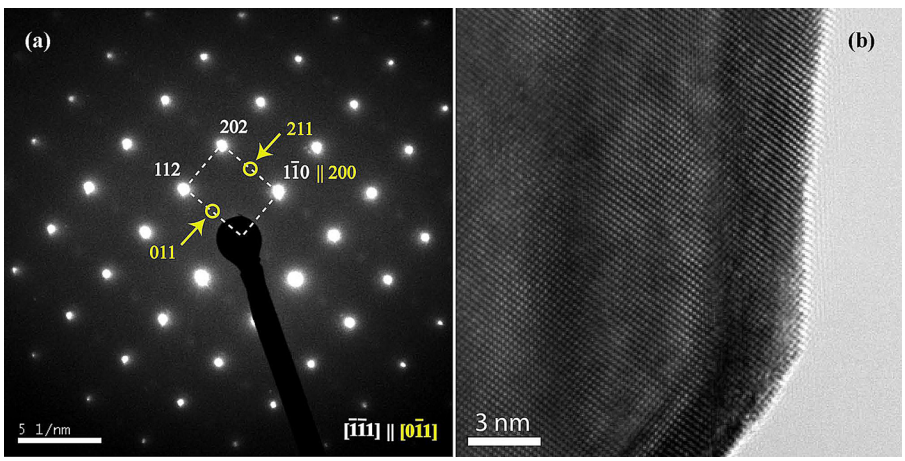


FIG. 3. (a) Main electron diffraction pattern of $EuTi(O,N)_{3\pm\delta}$ (white labels) and secondary pattern indicating a symmetry breaking (yellow labels). (b) High resolution micrograph of the same oriented grain.

[This article is copyrighted as indicated in the article. Reuse of AIP content is subject to the terms at: http://scitation.aip.org/termsconditions. Downloaded to ] IP: 134.94.122.242 On: Thu, 03 Apr 2014 08:07:48

Ti 2*p* and Eu 4*d* photoelectron peaks were studied in order to verify the oxidation state of the cations. Fig. 4(a) shows the deconvoluted Ti 2*p* doublet of $EuTi(O,N)_{3\pm\delta}$ with main peaks centered at $E_b = 457.5$ eV ($2p_{3/2}$) and $E_b = 463.3$ eV ($2p_{1/2}$). The shoulders at ~ 461.6 eV ($2p_{1/2}$) and ~ 455.8 eV ($2p_{3/2}$) are in agreement with published values of $Ti^{3+}$ (Ref. 38), indicating the existence of a minor content of $Ti^{3+}$ species. The $Ti^{3+}$ peak positions were inferred from the shoulders by deconvolution and Shirley-type background subtraction taking into account a fixed $2p_{3/2}$-to-$2p_{1/2}$ peak ratio of 3:2. The origin of $Ti^{3+}$ might be either caused by the TiN secondary phase or reduced Ti in the perovskite lattice. The small shoulder at 454.5 eV of Ti $2p_{3/2}$ can be assigned to $Ti^{2+}$. In Fig. 4(b), the Ti 2*p* spectrum of pristine $EuTiO_3$ (the precursor oxide) is compared to that of the oxynitride. The oxide spectrum is dominated by the $Ti^{4+}$ contribution but also shows the $Ti^{3+}$ shoulders. The Ti 2*p* signal of the oxynitride is shifted by about 0.8 eV to lower binding energies compared to the oxide due to the changed chemical environment of the titanium ions (different electronegativities of $O^{2-}$ and $N^{3-}$ ligands). Fig. 5(a) shows the Eu 4*d* XPS spectrum of $EuTi(O,N)_{3\pm\delta}$. The 4*d* multiplet structure of rare-earth elements with an unfilled 4*f* valence shell is complex due to the strong 4*d*-4*f* exchange interaction and a weaker spin-orbit splitting of the 4*d*

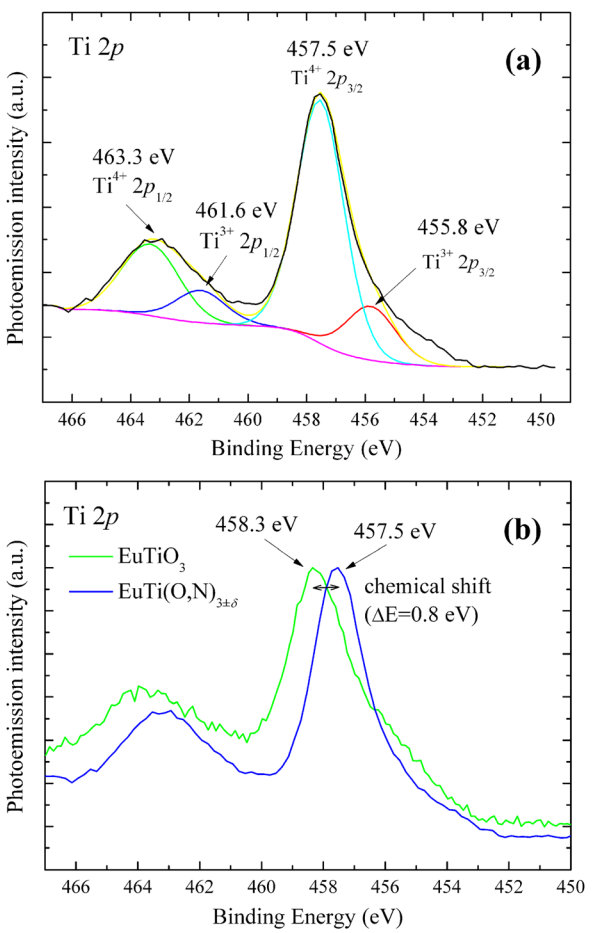


FIG. 4. (a) Deconvoluted Ti 2*p* XPS spectrum of $EuTi(O,N)_{3\pm\delta}$. (b) Comparison of Ti 2*p* XPS spectra of $EuTiO_3$ and $EuTi(O,N)_{3\pm\delta}$ normalized to the maximum.

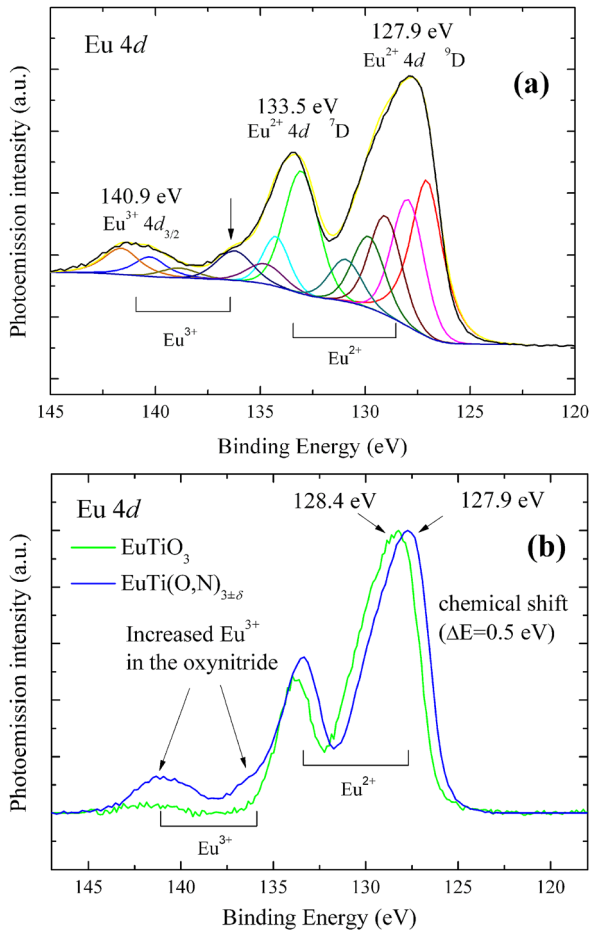


FIG. 5. (a) Eu 4*d* XPS multiplet of $EuTi(O,N)_{3\pm\delta}$ deconvoluted. (b) Eu 4*d* XPS spectrum of $EuTi(O,N)_{3\pm\delta}$ and $EuTiO_3$ normalized to the maximum.

orbitals.[39] The electrostatic interaction between 4*d* and 4*f* shell is large by reason of the same principal quantum number,[40] which is why the Eu 4*d* spectrum is not separated into its $4d_{3/2}$ and $4d_{5/2}$ components and the two main spectral contributions are assigned to $^7D$ and $^9D$ multiplets.[39] The main peaks are centered at $E_b = 127.9$ eV and $E_b = 133.5$ eV resulting from $Eu^{2+}$.[41] The fine structure of the $^9D$ peak was deconvoluted to its five components according to the electron spectroscopic theories for rare-earths detailed in Ref. 42 [Fig. 5(a)]. The $Eu^{3+}$ doublet is shifted by about 7 eV from $Eu^{2+}$ doublet to higher binding energies,[43] the main peak ($4d_{3/2}$) is at 140.9 eV and $4d_{5/2}$ is observable as a shoulder of $Eu^{2+}$ $^7D$ [indicated with an arrow in Fig. 5(a)]. For comparison, Eu 4*d* peak of $EuTiO_3$ is shown [Fig. 5(b)]. In accordance with the analysis of the titanium spectrum, the peaks of the oxynitride are slightly shifted to lower binding energies (~0.5 eV) due to the different electronic environment of Eu caused by the N present in the lattice. An increase of $Eu^{3+}$ is observed in $EuTi(O,N)_{3\pm\delta}$ compared with $EuTiO_3$ since the extra charge of $N^{-3}$ is balanced by an increased oxidation state of the Eu. The $Eu^{3+}/Eu^{2+}$ ratio was derived from the integrated spectral intensities (0.04 and 0.25 for $EuTiO_3$ and $EuTi(O,N)_{3\pm\delta}$, respectively).

The thermoelectric properties of the three different $EuTi(O,N)_{3\pm\delta}$ sample groups were studied and compared with the previously reported data of $EuTiO_3$.[12] The

[This article is copyrighted as indicated in the article. Reuse of AIP content is subject to the terms at: http://scitation.aip.org/termsconditions. Downloaded to ] IP: 134.94.122.242 On: Thu, 03 Apr 2014 08:07:48

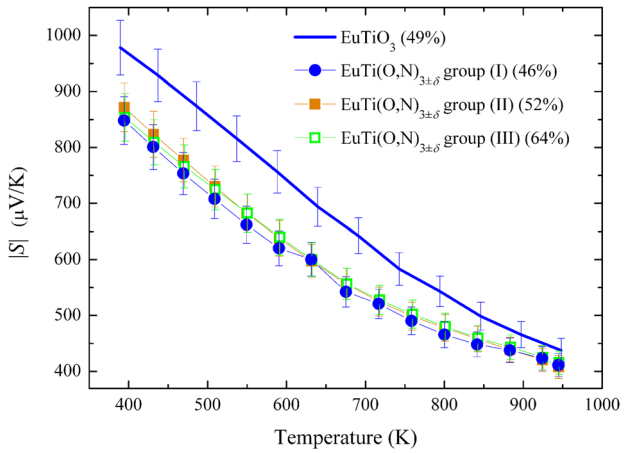


FIG. 6. Absolute value of the Seebeck coefficient ($S$) of the oxide and the three oxynitride pellets measured in the temperature range of 390 K–950 K.

atmosphere and maximum temperature used in the experiments were chosen after testing the thermal stability of the samples. The TGA study showed that $EuTi(O,N)_{3\pm\delta}$ is stable up to 992 K in reducing atmosphere while above this temperature mass reduction due to N loss in the form of $NH_3$ and $N_2$ was observed. The Seebeck coefficients ($S$) were measured in the temperature range of 390 K–950 K and found to be negative in the whole temperature range due to the $n$-type nature of the charge carriers. Fig. 6 shows the absolute value of the Seebeck coefficients for the three oxynitride pellets. Measurements on $EuTiO_3$ pellets of different porosity and equal composition revealed identical $S$ since it does not depend on the relative density but only on the electronic structure. Zhao *et al.*[44] also proved that the Seebeck coefficient of a porous and a fully dense bulk is equal and is related to the charge carrier concentration. The similar behavior of the $S$ of the three oxynitride groups indicates similar N contents, which was also confirmed by XPS analysis. For comparison, the $S$ values of $EuTiO_3$ are also plotted in Fig. 6. The lower $S$ of the oxynitrides compared to the oxide reveals a higher charge carrier concentration or a modified conduction mechanism in the oxynitrides. These results will be discussed and clarified later with the help of *ab initio* calculations.

The electrical resistivity ($\rho$) of the oxynitrides is higher than that of pristine [Fig. 7(a)], which can be attributed to the effect of the relative densities in the polycrystalline pellets. Samples (I) and (II) have the lowest relative densities (46% and 52%, respectively) and the highest $\rho$ (minimum values of 24.63 mΩ·m and 20.82 mΩ·m, respectively). Sample (III) has a higher density (64%), because it was pressed prior to ammonolysis, and its resistivity is lower (minimum value of 10.81 mΩ·m). The comparison of oxynitrides and oxide shows that the latter has an electrical resistivity nearly one order of magnitude lower despite its low relative density (49%). These results and the difficulty to densify oxynitrides suggest the presence of weak grain connectivity and intergrain transport in the oxynitride pellets. The error bars of $S$ and $\rho$ correspond to a 5% relative error and were calculated according to Ref. 45. The electrical resistivities of all the samples follow semiconductor-like

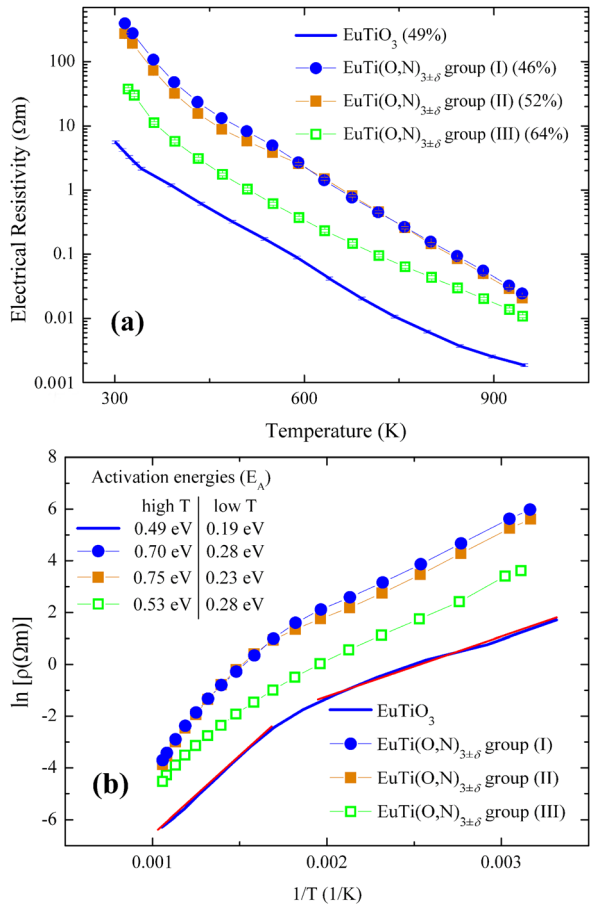


FIG. 7. (a) Electrical resistivity ($\rho$) of the oxide and oxynitride pellets measured in the temperature range of 300 K–950 K (error bars within the data points). (b) $\ln(\rho)$ vs. $1/T$ and calculated activation energies in the low temperature (extrinsic) and high temperature (intrinsic) regimes.

dependence with temperature. In Fig. 7(b), we plotted $\ln(\rho)$ against $1/T$ and extracted the activation energies ($E_A$) from the slopes of the curves using Arrhenius formula [$\rho = \rho_0 \exp(E_A/k_BT)$, where $\rho_0$ is a pre-exponential constant and $k_B$ is the Boltzmann constant]. The change in the slope of the curves indicates that there are two regimes distinguishable for all the samples: extrinsic and intrinsic semiconducting behavior at low and high temperatures, respectively. At high temperatures (intrinsic regime) the activation energy equals half the fundamental band gap energy ($E_g$). Therefore, we can calculate $E_g$ of the samples from the activation energy in the intrinsic regime ($E_g = 2E_A$). First, we extracted the band gap of $EuTiO_3$: $E_g = 2E_A = 0.98$ eV, where $E_A = 0.49$ eV, which is in agreement with the value $E_g = 0.93 \pm 0.07$ eV reported for room temperature in Ref. 46. The transition temperature between extrinsic and intrinsic regimes of the pristine $EuTiO_3$ was determined to be around 540 K and the activation energy calculated for low temperature is $E_A = 0.19$ eV, significantly smaller than for the high temperature regime due to localized in-gap or donor states. The extrinsic (low temperature) activation energies calculated for the oxynitride samples is $E_A = 0.28$; 0.23; 0.28 eV for groups (I), (II), and (III), respectively. The transition temperatures between extrinsic and intrinsic conducting regimes were approximated to be around 610 K for oxynitride groups (I)

[This article is copyrighted as indicated in the article. Reuse of AIP content is subject to the terms at: http://scitation.aip.org/termsconditions. Downloaded to ] IP: 134.94.122.242 On: Thu, 03 Apr 2014 08:07:48

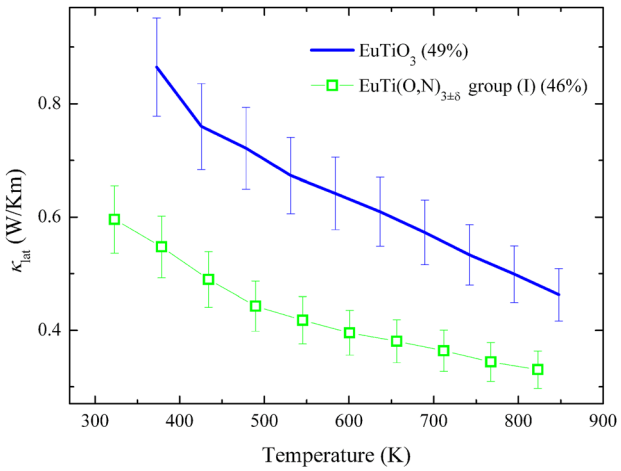


FIG. 8. Lattice thermal conductivity ($\kappa_{lat}$) of the oxynitride and the oxide in the temperature range of 330 K–850 K.

and (II), and 570 K for group (III). In the intrinsic regime (high temperature), $E_A$ values for samples (I) and (II) are very similar: $E_A = 0.70$ eV and 0.75 eV, respectively, while group (III) has smaller intrinsic activation energy ($E_A = 0.53$ eV). The calculated band gaps for the oxynitrides are: $E_g = 1.40$ eV, 1.50 eV, and 1.06 eV for groups (I), (II), and (III), respectively. The lower $E_g$ value of group (III) can be related to its higher relative density and therefore less defective morphology. The weak grain connectivity of oxynitrides (I) and (II) strongly influences the electrical resistivity measurement, and therefore *ab initio* calculations of the electronic structures will be shown in order to relate the experimental values to the theoretical ones. Overall, the band gap $E_g$ of the oxynitrides is higher than that of pristine, which explains the higher $\rho$ measured and will also be compared with our *ab initio* calculations.

The total thermal conductivity ($\kappa$) is the sum of the electronic ($\kappa_{el}$) and the lattice part ($\kappa_{lat}$). The electronic contribution can be approximated using the Wiedemann-Franz law: $\kappa_{el} = L_0 T/\rho$, where $L_0$ ($= 2.443 \cdot 10^{-8}$ W $S^{-1}K^{-2}$) is the Lorenz number for the free electron gas. Fig. 8 shows the lattice contribution of $\kappa$ of the oxynitride [group (I); 46% relative density] and the oxide (49% relative density) in the temperature range of 330 K < T < 850 K. Above room temperature, $\kappa_{lat}$ of both samples decreases proportional to 1/T due to the increasing amount of phonons available to participate in the Umklapp scattering. $\kappa_{lat}$ of the oxynitride is lower than that of the oxide because of its lower relative density. Morphology and grain interconnectivity of the pellets must be analyzed in order to comprehensively assess the transport properties. The error bar of $\kappa_{lat}$ is of 10% relative error and was calculated according to Ref. 45.

The morphology of the particles was studied by TEM and the influence of nitridation on the grains of the sintered samples by SEM. TEM micrographs of $EuTi(O,N)_{3 \pm \delta}$ and $EuTiO_3$ particles are shown in Figs. 9(a) and 9(c), respectively. The oxide forms large crystallites with grain sizes of 0.2–1 $\mu$m, while the oxynitride consist of pores and particles with mean grain size of only 0.1–0.8 $\mu$m. The formation of porous grains after ammonolysis has been observed in previous studies like in the case of $LaTaON_2$ by Park and Kim.[21] During ammonolysis, nitrogen diffuses into the oxide structure creating open paths or voids which allow $3O^{2-} \rightarrow 2N^{3-}$ exchange, resulting in pores with mean sizes of 10–40 nm. During sintering in ammonia, the described process of N incorporation leads to an inefficient sintering of the particles and restricts the interconnection of the grains, as shown in

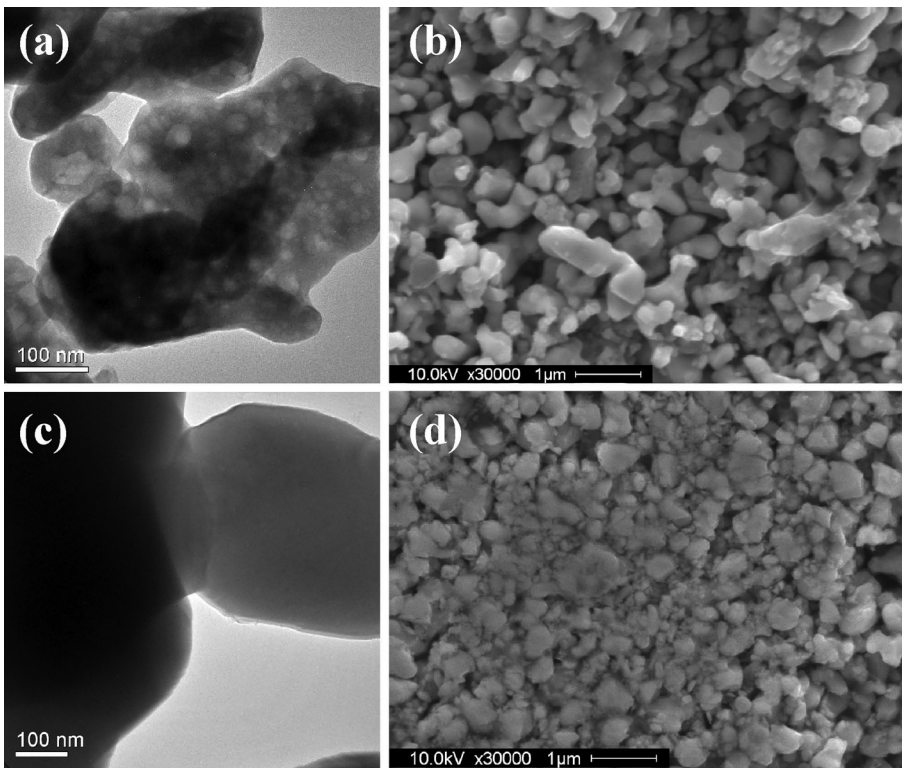


FIG. 9. TEM micrographs of (a) $EuTi(O,N)_{3 \pm \delta}$ and (c) $EuTiO_3$ powder particles, and SEM (SE) micrographs of (b) $EuTi(O,N)_{3 \pm \delta}$ (I) and (d) $EuTiO_3$ sintered pellets.

[This article is copyrighted as indicated in the article. Reuse of AIP content is subject to the terms at: http://scitation.aip.org/termsconditions. Downloaded to ] IP: 134.94.122.242 On: Thu, 03 Apr 2014 08:07:48

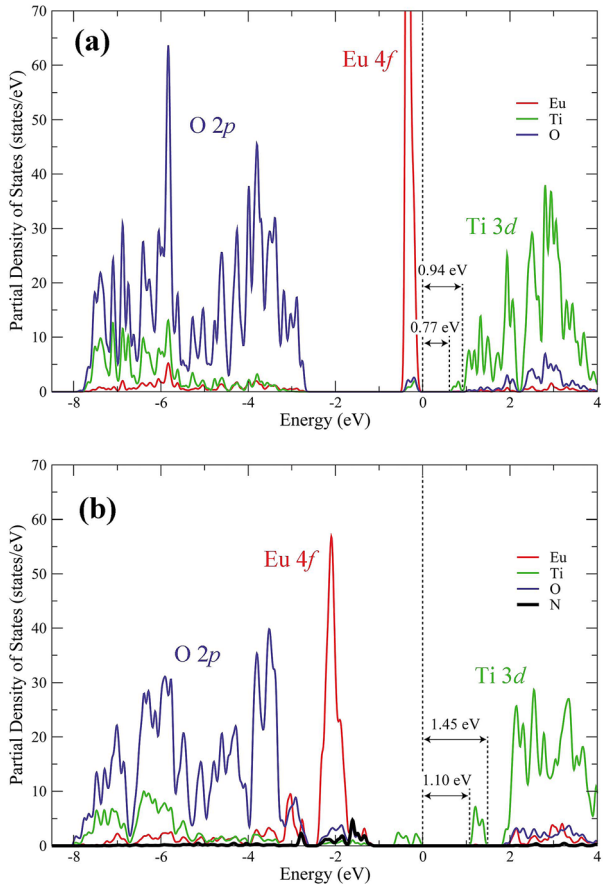


FIG. 10. Partial electronic density of states of (a) pristine $EuTiO_3$ and (b) nitrogen substituted $EuTi(O,N)_{3\pm\delta}$. The zero level of energy was chosen as the top of the valence band.

Fig. 9(b). The micrograph presents well defined grain boundaries and low connectivity between the grains. For comparison, a sintered pellet of $EuTiO_3$ with well fused grains is shown in Fig. 9(d). In this case, no sharp grain boundaries appear in the image due to intergrowth effects of the intergrains. This is a clear evidence of the complex particle morphology and the limited grain connectivity of the oxynitride samples. The Seebeck coefficient remains unaffected by the porosity, but the electrical conductivity, as well as the thermal conductivity, is lowered by the poor grain interconnectivity. While low $\kappa$ is beneficial for a good thermoelectric performance, a limited electrical conductivity is unfavorable and therefore the $ZT$ measured for $EuTi(O,N)_{3\pm\delta}$ [group (I)] was only $ZT = 0.004$ at 820 K.

*Ab initio* calculations were performed for a better understanding of the experimental results. Fig. 10(a) shows the partial electronic density of states of pristine $EuTiO_3$. The bottom of the conduction band (CB) is formed by Ti 3*d* states. There is a small localized peak split-off from the rest of the conduction band (donor-like band), situated at $E_d = 0.77$ eV. The bottom of the CB is situated at $E_c = 0.94$ eV, which corresponds also to the value of the fundamental band gap ($E_g$). This is in a very good agreement with the $E_g = 2E_A = 0.98$ eV extracted from the experimental electrical resistivity data [see Fig. 7(b)] and with the gap $E_g = 0.93$ eV measured by Lee *et al.*[46] The presence of localized donor-like states close to the bottom of the CB probably leads to the tail in the absorption spectra in the vicinity of the fundamental gap observed in Ref. 46. If we assume a doped, non-degenerate and compensated semiconductor the activation energy at low temperatures equals the ionization energy: $E_A = E_c - E_d$. The result that we obtain from the calculation of the DOS, $E_A = 0.94 - 0.77 = 0.17$ eV, is in good agreement with the extrinsic activation energy (low temperatures) extracted from our electrical resistivity measurement: $E_A = 0.19$ eV [Fig. 7(b)]. The top of the valence band (VB) is formed by strongly localized Eu 4*f* orbitals, with small admixture of O 2*p* and Ti 3*d* states, which mediate the magnetic interaction between $Eu^{2+}$ 4*f* spins via 3*d* states of nonmagnetic $Ti^{4+}$.[47] The bulk of the VB is formed mainly by oxygen 2*p* states, and is located about 3 eV below the top of the valence band.

The electronic structure is drastically changed by tilting of the anion octahedra in the *Pnma* structure of $EuTi(O,N)_{3\pm\delta}$ [see Fig. 10(b)]. At the bottom of the CB there is a split-off donor-like band similar to the case of $EuTiO_3$, which is formed by equal contribution of all Ti 3*d* atoms. In this case, the split-off has a larger contribution to the density of states and is wider in the energy spectrum, i.e., it is more delocalized compared to the split-off of the pristine compound. Therefore, the theoretical band gap of $EuTi(O,N)_{3\pm\delta}$ is the distance from the top of the VB to the beginning of donor-like band ($E_g = 1.10$ eV). The experimental values of $E_g$ extracted from Arrhenius formula are different for different relative densities of the oxynitride samples [$E_g = 1.40$ eV, 1.50 eV, and 1.06 eV for groups (I), (II), and (III), respectively] and they all lie approximately within the energy width of the donor-like band (localized between 1.10 and 1.45 eV). The samples with lower relative densities [groups (I) and (II)] are more defective and show higher values of $E_g$ due to the presence of defect states at the lower energy levels of the donor-like band. Sample (III) is less defective (larger relative density) and its experimental band gap ($E_g = 1.06$ eV) coincides with the energy of the beginning of the donor-like band. The middle point of this band is at $E_d = 1.28$ eV and the bottom of the rest of the CB starts at $E_c = 1.84$ eV. The case of the oxynitride follows the model of doped, non-degenerate and uncompensated semiconductors, where the activation energy at low temperatures equals half the ionization energy: $E_A = (E_c - E_d)/2$. The $E_A$ value obtained from the *ab initio* calculations $E_A = (1.84 - 1.28)/2 = 0.28$ eV agrees with the extrinsic activation energies (low temperature regime) of the oxynitrides deduced from the electrical resistivity measurement: $E_A = 0.23$, 0.28 eV [Fig. 7(b)]. The top of the valence band and the bottom of the conduction band are formed by localized Ti 3*d* states. Here, we should note that the top-VB states are built by those Ti atoms far apart from the N atoms as it is represented in Fig. 11(a). Fig. 11(a) shows the electronic charge distribution of the top of the VB. Ti atoms far from N (atoms 3 and 4) present a higher charge density contribution than the neighboring Ti atoms (atoms 1 and 2). The observed DOS at the VB is therefore caused by the tilting of the $TiO_6$ octahedra and is not directly related to the N "impurity" states. One of the main differences in the spectra of pristine and ammonolyzed $EuTiO_3$ is the position of the Eu 4*f* states:

[This article is copyrighted as indicated in the article. Reuse of AIP content is subject to the terms at: http://scitation.aip.org/termsconditions. Downloaded to ] IP: 134.94.122.242 On: Thu, 03 Apr 2014 08:07:48

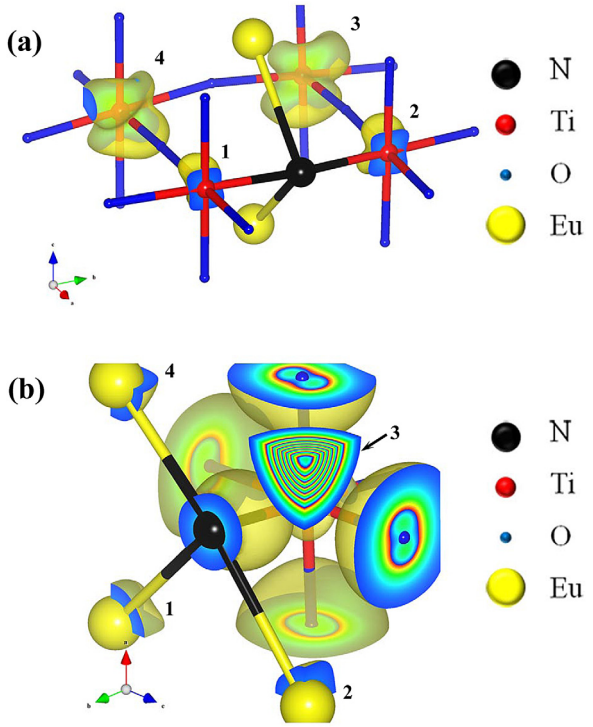


FIG. 11. (a) Electronic charge density distribution of the top of the VB (energy range: −1 to 0 eV) (b) and section of Eu-N bonds in the energy region −4 to −2.64 eV. These numbers correspond to the energy scale of Fig. 10(b). The isosurfaces of the charge density plots were 0.01 and 0.05 $e^-/Å^3$ for figures (a) and (b), respectively. The contours at the sections are plotted with color code blue-green-red covering the interval from 0 to 0.2 $e^-/Å^3$ for figure (a) and from 0 to 1 $e^-/Å^3$ for figure (b).

in the *Pnma* structure of the oxynitride they are shifted by about 2 eV to lower energies and almost merge with the oxygen 2*p* states in the bulk of the valence band. Also, tilting of the anion octahedra in the *Pnma* structure causes delocalization of the states in the Eu 4*f* shell resulting in the broadening of the corresponding peak. The nitrogen "impurity" states are located at same energy region as the Eu 4*f* states (near −2 eV). Four of the Eu atoms are the first nearest neighbors around the nitrogen "impurity." An important feature of the spectrum is a peak formed by N 2*p* and Eu 4*f* states at around −2.8 eV below the top of the valence band. The contribution of Eu to the density of states is attributed to one of the four Eu atoms from nitrogen vicinity (Eu atom number 3) as shown in Fig. 11(b). This feature reflects a covalent-like interaction with charge transfer from Eu towards N: the corresponding Eu cation has 0.1|*e*| less charge on *f*-shell and 0.05|*e*| more on *d* shell than the rest of the Eu cations. This is consistent with the observed increase of $Eu^{3+}$ content of the oxynitrides [see Fig. 5(b)].

A more detailed comparison of the total density of states (DOS) for pristine and ammonolyzed $EuTiO_3$ is shown in Fig. 12. As it was noted above, the most significant difference is observed at the top of the valence band. It is beneficial for a high Seebeck coefficient to have a high DOS just below $E_F$ since $S \propto [\partial \ln n(E)/\partial E]_{E=E_F}$.[48] The Eu 4*f* peak of $EuTi(O,N)_{3\pm\delta}$ is shifted further away from the top of the VB compared to $EuTiO_3$ due to the structural change from cubic to orthorhombic. In addition, the intensity of the Eu 4*f*

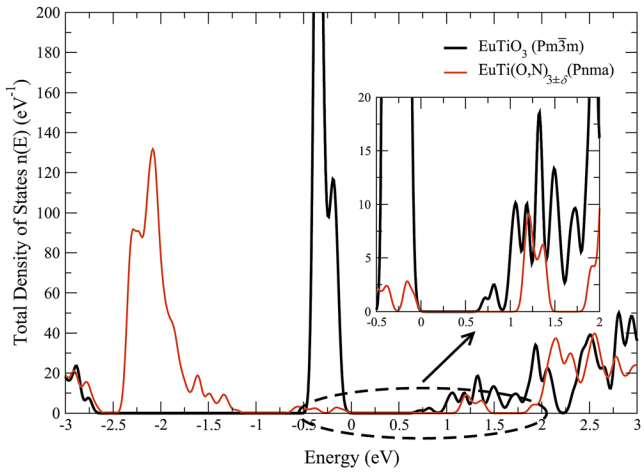


FIG. 12. Comparison of the total density of states of $EuTi(O,N)_{3\pm\delta}$ and $EuTiO_3$. The zero level of energy was chosen as the top of the valence band.

peak of $EuTi(O,N)_{3\pm\delta}$ is much lower than that of $EuTiO_3$, which would also explain its lower Seebeck coefficient (Fig. 6). The calculated band gap of the oxynitride is slightly larger than of the oxide, which is also consistent with the higher electrical resistivity of the oxynitride compared to the pristine compound.

## V. CONCLUSIONS

$EuTi(O,N)_{3\pm\delta}$ powders were produced by thermal ammonolysis of the precursor oxide. It was proven by neutron and electron diffractions that with the incorporation of nitrogen the space group changes from cubic $Pm\bar{3}m$ to orthorhombic *Pnma*. The N content of pellets produced by the three different routes was determined by XPS analysis of the N 1*s* peak. All samples had similar N contents being slightly lower for sample (III). TGA analysis showed stability up to 992 K in reducing atmosphere, and thus, the thermoelectric properties were measured from room temperature up to 950 K. The lower *S* of the oxynitrides compared with the oxide suggested a higher charge carrier concentration of the oxynitrides. Electrical resistivity measurements showed higher conductivity and lower band gap for the pristine sample than for the poorly sintered oxynitrides. Morphological studies using SEM proved low grain connectivity of the oxynitride pellets. TEM analysis of the powders showed a complex structure with intrinsic nanopores within the oxynitride particles, and large and crystalline oxide particles. The introduction of nitrogen into the oxide prevents the formation of large crystallites and consequently the fusion of grains, which affects the electrical and thermal transport. The lattice thermal conductivity of pristine $EuTiO_3$ was reduced from 0.87 W/Km to 0.55 W/Km after nitridation (at 370 K). Calculations of the DOS of $EuTi(O,N)_{3\pm\delta}$ and $EuTiO_3$ confirmed the larger band gap of the distorted crystal structure compared with the oxide. The change on the shape of the VB is a consequence of the octahedral tilting, since it is formed by the Ti atoms which are far from N. The shift and the intensity decrease of the Eu 4*f* peak explained the lower values of Seebeck coefficients of $EuTi(O,N)_{3\pm\delta}$.

[This article is copyrighted as indicated in the article. Reuse of AIP content is subject to the terms at: http://scitation.aip.org/termsconditions. Downloaded to ] IP: 134.94.122.242 On: Thu, 03 Apr 2014 08:07:48

## ACKNOWLEDGMENTS

Financial support from SNF (Swiss National Science Foundation) within the National Centre of Competence in Research (NCCR) "MaNEP – Materials with Novel Electronic Properties" is highly acknowledged. Neutron diffraction was performed at the Swiss Spallation Neutron Source SINQ, at the Paul Scherrer Institut, Villigen, Switzerland (proposal-number 20100537). The authors thank Dr. Denis Sheptyakov for helpful discussion and support during the neutron measurement campaign. This work was also supported by the Young Investigators Group Program of the Helmholtz Association, Germany (contract VH-NG-409), the Jülich Supercomputer Centre, and the Empa Electron Microscopy Center.

[1]R. Ranjan, H. Sadat Nabi, and R. Pentcheva, J. Phys.: Condens. Matter **19**, 406217 (2007).
[2]S. Kamba, D. Nuzhnyy, P. Vaněk, M. Savinov, K. Knížek, Z. Shen, E. Šantavá, K. Maca, M. Sadowski, and J. Petzelt, EPL **80**, 27002 (2007).
[3]V. Goian, S. Kamba, O. Pacherová, J. Drahokoupil, L. Palatinus, M. Dušek, J. Rohlíček, M. Savinov, F. Laufek, W. Schranz, A. Fuith, M. Kachlík, K. Maca, A. Shkabko, L. Sagarna, A. Weidenkaff, and A. Belik, Phys. Rev. B **86**, 054112 (2012).
[4]T. Katsufuji and H. Takagi, Phys. Rev. B **64**, 054415 (2001).
[5]T. R. McGuire, M. W. Shafer, R. J. Joenk, H. A. Alperin, and S. J. Pickart, J. Appl. Phys. **37**, 981 (1966).
[6]M. Allieta, M. Scavini, L. Spalek, V. Scagnoli, H. C. Walker, C. Panagopoulos, S. Saxena, T. Katsufuji, and C. Mazzoli, Phys. Rev. B **85**, 184107 (2012).
[7]K. Rushchanskii, N. Spaldin, and M. Ležaić, Phys. Rev. B **85**, 104109 (2012).
[8]S. Kamba, V. Goian, M. Orlita, D. Nuzhnyy, J. H. Lee, D. G. Schlom, K. Z. Rushchanskii, M. Ležaić, T. Birol, C. J. Fennie, P. Gemeiner, B. Dkhil, V. Bovtun, M. Kempa, J. Hlinka, and J. Petzelt, Phys. Rev. B **85**, 094435 (2012).
[9]Z. Guguchia, A. Shengelaya, H. Keller, J. Köhler, and A. Bussmann-Holder, Phys. Rev. B **85**, 134113 (2012).
[10]A. O. Sushkov, S. Eckel, and S. K. Lamoreaux, Phys. Rev. A **81**, 022104 (2010).
[11]K. Z. Rushchanskii, S. Kamba, V. Goian, P. Vaněk, M. Savinov, J. Prokleška, D. Nuzhnyy, K. Knížek, F. Laufek, S. Eckel, S. K. Lamoreaux, A. O. Sushkov, M. Ležaić, and N. A. Spaldin, Nature Mater. **9**, 649 (2010).
[12]L. Sagarna, A. Shkabko, S. Populoh, L. Karvonen, and A. Weidenkaff, Appl. Phys. Lett. **101**, 033908 (2012).
[13]A. Fuertes, Dalton Trans. **39**, 5942 (2010).
[14]A. Fuertes, J. Mater. Chem. **22**, 3293 (2012).
[15]S. G. Ebbinghaus, H.-P. Abicht, R. Dronskowski, T. Müller, A. Reller, and A. Weidenkaff, Prog. Solid State Chem. **37**, 173 (2009).
[16]A. Kusmartseva, M. Yang, J. Oró-Solé, A. M. Bea, A. Fuertes, and J. P. Attfield, Appl. Phys. Lett. **95**, 022110 (2009).
[17]Y.-I. Kim, P. M. Woodward, K. Z. Baba-Kishi, and C. W. Tai, Chem. Mater. **16**, 1267 (2004).
[18]A. Maegli, S. Yoon, E. Otal, L. Karvonen, P. Mandaliev, and A. Weidenkaff, J. Solid State Chem. **184**, 929 (2011).
[19]M. Yang, J. Oró-Solé, J. A. Rodgers, A. B. Jorge, A. Fuertes, and J. P. Attfield, Nat. Chem. **3**, 47 (2011).
[20]A. Hellwig and A. Hendry, J. Mater. Sci. **29**, 4686 (1994).
[21]N.-Y. Park and Y.-I. Kim, J. Mater. Sci. **47**, 5333 (2012).
[22]A. Le Bail, H. Duroy, and J. L. Fourquet, Mater. Res. Bull. **23**, 447 (1988).
[23]H. M. Rietveld, J. Appl. Crystallogr. **2**, 65 (1969).
[24]J. Rodríguez-Carvajal, Physica B **192**, 55 (1993).
[25]P. Thompson, D. E. Cox, and J. B. Hastings, J. Appl. Crystallogr. **20**, 79 (1987).
[26]G. Kresse and J. Hafner, Phys. Rev. B **47**, 558 (1993).
[27]G. Kresse, Phys. Rev. B **54**, 11169 (1996).
[28]P. E. Blöchl, Phys. Rev. B **50**, 17953 (1994).
[29]J. Heyd, G. E. Scuseria, and M. Ernzerhof, J. Chem. Phys. **118**, 8207 (2003).
[30]J. P. Perdew, K. Burke, and M. Ernzerhof, Phys. Rev. Lett. **77**, 3865 (1996).
[31]H. J. Monkhorst and J. D. Pack, Phys. Rev. B **13**, 5188 (1976).
[32]S. G. Ebbinghaus, A. Weidenkaff, A. Rachel, and A. Reller, Acta Crystallogr., Sect. C: Cryst. Struct. Commun. **60**, i91 (2004).
[33]D. L. Bish and S. A. Howard, J. Appl. Crystallogr. **21**, 86 (1988).
[34]T. Motohashi, Y. Hamade, Y. Masubuchi, T. Takeda, K. Murai, A. Yoshiasa, and S. Kikkawa, Mater. Res. Bull. **44**, 1899 (2009).
[35]K. Tanaka and Y. Ōnuki, Acta Crystallogr., Sect. B: Struct. Sci. **58**, 423 (2002).
[36]Z. Zhang, X. Wang, J. Long, Q. Gu, Z. Ding, and X. Fu, J. Catal. **276**, 201 (2010).
[37]G. Koster, B. L. Kropman, G. J. H. M. Rijnders, D. H. A. Blank, and H. Rogalla, Appl. Phys. Lett. **73**, 2920 (1998).
[38]K.-Y. Yang, K.-Z. Fung, and M.-C. Wang, J. Appl. Phys. **100**, 056102 (2006).
[39]C. Caspers, M. Müller, A. X. Gray, A. M. Kaiser, A. Gloskovskii, C. S. Fadley, W. Drube, and C. M. Schneider, Phys. Status Solidi (RRL) **5**, 441 (2011).
[40]H. Ogasawara, A. Kotani, and B. Thole, Phys. Rev. B **50**, 12332 (1994).
[41]C. Laubschat, B. Perscheid, and W. Schneider, Phys. Rev. B **28**, 4342 (1983).
[42]C. Gerth, A. Kochur, M. Groen, T. Luhmann, M. Richter, and P. Zimmermann, Phys. Rev. A **57**, 3523 (1998).
[43]W.-D. Schneider, C. Laubschat, I. Nowik, and G. Kaindl, Phys. Rev. B **24**, 5422 (1981).
[44]L. D. Zhao, B.-P. Zhang, W. S. Liu, H. L. Zhang, and J.-F. Li, J. Alloys Compd. **467**, 91 (2009).
[45]S. Populoh, M. H. Aguirre, O. C. Brunko, K. Galazka, Y. Lu, and A. Weidenkaff, Scr. Mater. **66**, 1073 (2012).
[46]J. H. Lee, X. Ke, N. J. Podraza, L. F. Kourkoutis, T. Heeg, M. Roeckerath, J. W. Freeland, C. J. Fennie, J. Schubert, D. A. Muller, P. Schiffer, and D. G. Schlom, Appl. Phys. Lett. **94**, 212509 (2009).
[47]H. Akamatsu, Y. Kumagai, F. Oba, K. Fujita, H. Murakami, K. Tanaka, and I. Tanaka, Phys. Rev. B **83**, 214421 (2011).
[48]N. F. Mott and E. A. Davis, *Electronic Processes in Non-Crystalline Materials* (Oxford University Press, Oxford, 2012).

[This article is copyrighted as indicated in the article. Reuse of AIP content is subject to the terms at: http://scitation.aip.org/termsconditions. Downloaded to ] IP: 134.94.122.242 On: Thu, 03 Apr 2014 08:07:48